Contents lists available at ScienceDirect

Applied Catalysis B: Environmental

High photocatalytic hydrogen production on Cu(II) pre-grafted Pt/TiO$_2$

Maria Vittoria Dozzi [a],[*], Gian Luca Chiarello [a],[b], Matteo Pedroni [a], Stefano Livraghi [c], Elio Giamello [c], Elena Selli [a]

[a] Dipartimento di Chimica, Università degli Studi di Milano, via Golgi 19, I-20133 Milano, Italy
[b] Empa, Swiss Federal Laboratories for Materials Science and Technology, Ueberlandstrasse 129, CH-8600 Dübendorf, Switzerland
[c] Dipartimento di Chimica, Università degli Studi di Torino, via Giuria 7, I-10125 Torino, Italy

ARTICLE INFO

ABSTRACT

A series of Pt/Cu/TiO$_2$ photocatalysts, showing very high performance in photocatalytic hydrogen production from methanol/water vapour mixtures, were prepared under mild conditions by Cu(II) grafting on commercial P25 TiO$_2$, with nominal Cu/TiO$_2$ ratios ranging from 0.05 to 0.5 wt.%, followed by 0.5 wt.% Pt nanoparticles deposition by the deposition-precipitation method in the presence of urea. The structural features of the so obtained materials were fully characterized by X-ray absorption spectroscopy, which provided information on the oxidation state of the two metals and on the metal–metal and metal-TiO$_2$ interactions, and by EPR analysis, which evidenced electron transfer phenomena involving copper under irradiation. The photocatalysts showed a volcano-shaped photoactivity trend in hydrogen production with increasing nominal Cu content, the maximum rate of H$_2$ evolution (27.2 mmol h^{-1} g$_{cat}$$^{-1}$) being attained with the photocatalyst containing 0.1 wt.% of copper. In this sample CuO nanoclusters appear to be intimately coordinated with surface Ti atoms in a surface structure that partially stabilizes pre-grafted copper in metallic form, possibly acting as an electron-transfer bridge at the interface between CuO nanoclusters and TiO$_2$. Synergistic effects in H$_2$ photocatalytic production are clearly induced by the co-presence of grafted Cu nanoclusters and Pt nanoparticles on the TiO$_2$ surface, with the copper oxidation state switching under UV–vis irradiation, facilitating electron transfer to adsorbed protons.

© 2017 Elsevier B.V. All rights reserved.

1. Introduction

With the present urgent demand for clean energy production from renewable sources, heterogeneous photocatalysis confirms to be an environmentally friendly method to produce hydrogen, the most attractive energy vector for the future. Amongst the possible photocatalytic materials for this application, titanium dioxide still remains the most employed and investigated semiconductor oxide photocatalyst, mainly because of its peculiar physical and chemical properties [1], although encouraging results have been recently obtained also employing carbon nitride-based photocatalysts [2,3]. However, the fruitful exploitation of solar light to directly split pure water into H$_2$ and O$_2$, with zero CO$_2$ emission, needs to face with both the high Gibbs free energy associated to such process (+237 kJ mol^{-1}, 1.23 eV) and the fast back-reaction occurring between the two gas products [4]. Moreover, photocatalytic H$_2$ production does not efficiently proceed on bare TiO$_2$, mainly due to the rapid recombination of photoproduced electron-hole pairs, which largely reduces the fraction of photogenerated charge carriers effectively involved in this thermodynamically up-hill reaction.

The addition of organic compounds, possibly deriving from renewable sources (i.e. biomass), to the aqueous reaction media proved to be successful to overpass such limitations [5]. In fact, organic molecules, such as alcohols, are not only additional proton sources, but also efficient hole scavengers which undergo fast and irreversible oxidation, thus making photopromoted electrons more readily available for proton reduction to hydrogen [6]. The separation of photoproduced charge carriers can be further increased by loading noble metal (i.e. Pt, Pd, Au) nanoparticles (NPs) on the semiconductor surface, because of their ability to capture photo-promoted electrons [7,8]. Platinum is considered the most effective co-catalyst to improve the photocatalytic efficiency of TiO$_2$, but its high cost may strongly limit the widespread use of Pt/TiO$_2$ photocatalytic materials, especially for industrial applications. Many efforts have thus been recently directed towards TiO$_2$ surface modification with less expensive metals (e.g., Cu, Ni, Ag), eventually coupled with low amounts of noble metal NPs, to increase the photoactivity in both wastewater treatments (organic pollutants

degradation) [9,10] and H_2 evolution from water [11]. For instance, the co-deposition of Au NPs together with Ni or Cu NPs, anchored on TiO_2 in different oxidation states, produced an effective increase of the photocatalytic production of H_2 with respect to that attained with Au/TiO_2 materials [12]. Very recently, TiO_2 surface modified with radiolysis-synthesized nickel and gold NPs was found to have synergistic effects in increasing the rate of H_2 formation from aqueous methanol solutions [13].

The use of Cu as relatively cheap and abundant co-catalyst can lead to highly efficient TiO_2-based photocatalysts. Starting from the pioneering work by Irie et al. [14], grafting of Cu^{2+} ions mainly on rutile TiO_2 was successfully applied to get visible light activation of the semiconductor without introducing impurity levels into the bulk of TiO_2 and beneficial effects were attained not only in the photodecomposition of air pollutants (*e.g.* acetaldehyde) or in antibacterial applications under *aerobic* conditions, but also in H_2 evolution under *anaerobic* conditions, with results superior to those obtained with Ni-loaded TiO_2 [15]. In fact, since both the redox potential of the Cu^{2+}/Cu^+ couple and the potential of the conduction band (CB) of crystalline CuO are less negative than the CB of TiO_2, CuO domains on the TiO_2 surface may capture photoexcited electrons with the consequent partial reduction of copper and beneficial charge carriers separation [16].

The activity of Cu-containing TiO_2-based photocatalysts was found to be affected by different properties such as the oxidation state of copper, the dispersion and morphology of metal and/or metal oxide NPs on the TiO_2 surface, including the crystallinity [17] and size of CuO clusters [18], as well as by the phase composition of TiO_2 [19]. Such key parameters can be modulated during the photocatalyst preparation and innovative synthetic routes were developed to this aim, including the use of water-in-oil microemulsions [20] or solvothermal microwave procedures [21].

At the same time, too high copper loading and calcination temperature, which are generally employed to get a solid CuO/TiO_2 heterojunction, favour the formation of large CuO_x deposits, with relatively low amount of metallic copper and detrimental effects on photoactivity [22]. Recently, hybrid TiO_2 based materials modified with both Cu and Pt were found to photogenerate H_2 with higher efficiency with respect to the monometallic counterparts [23]. In general, bimetallic Cu-Pt co-catalysts were synthetized with the aim of obtaining alloys, and also to exploit their plasmonic activation under visible light irradiation and aerobic oxidation conditions [24].

In the present work we explore the effects that pre-grafting TiO_2 with different amounts of Cu(II), followed by Pt NPs deposition, has on its photoactivity in hydrogen production. Mild deposition conditions were employed, with the two metal precursors being contacted with the TiO_2 powders in subsequent steps and no high temperature treatment, aiming at avoiding possible metal alloying and/or doping within the TiO_2 lattice. A thorough X-ray absorption analysis, providing information on the oxidation state of the two metals and on the metal–metal and metal-TiO_2 interactions for different Cu/Pt ratios, and EPR analysis, evidencing electron transfer phenomena occurring under irradiation, were employed for the interpretation of the synergistic effects in photoactivity obtained in H_2 production from methanol/water vapour mixtures with our Pt/Cu-modified TiO_2 materials.

2. Experimental section

2.1. Photocatalysts preparation

All photocatalysts were prepared starting from Evonik P25 TiO_2, directly employed as supplied. Pt/Cu/TiO_2 materials were prepared by grafting Cu(II) metal ions on the TiO_2 surface (step A), followed by Pt NPs deposition (step B). $Cu(NO_3)_2 \cdot 3H_2O$ was the Cu(II) source in the first step. In a typical grafting procedure, 2 g of P25 TiO_2 powder were dispersed in 20 mL of water and sonicated for 10 min in a FALC LBS2 4.5 L bath. Then a proper amount of $Cu(NO_3)_2 \cdot 3H_2O$ was dissolved in 1.0 mL of water and mixed with the aqueous TiO_2 suspension in a vial. The mixture was heated at 90 °C for 1 h under stirring, up to complete solvent removal. The so obtained materials were then dried at 110 °C for 24 h and ground into fine powders using an agate mortar. They were labelled as Cu(X)/T, with X corresponding to the nominal Cu/TiO_2 ratio, ranging from 0.05 to 0.5 wt.%.

In the second step such samples were further surface modified by deposition of a fixed amount (0.5 wt.%) of Pt NPs according to a modified version of the deposition-precipitation (DP) method, using urea as the precipitating agent [25]. In particular, an aliquot of a Cu(X)/T sample was suspended in water, sonicated and added to an aqueous solution containing H_2PtCl_6 (0.1 g L^{-1} of Pt) and urea (0.42 M). The suspension was vigorously stirred for 4 h at 80 °C, until pH 7.5 was reached. The slurry was then cooled down to room temperature and the precipitate was collected by centrifugation, using a CL10 Thermo Scientific centrifuge. The solid product was then re-suspended in 20 mL of water and platinum was reduced by addition of an aqueous $NaBH_4$ solution in slight excess. The color of the suspension suddenly changed from white or slightly green into grey. After 20 min stirring, the slurry was centrifuged and the solid recovered and washed several times with 20 mL of water, until the residual content of chloride and nitrate anions in the supernatant was below 1 ppm, as checked by ion chromatography. The so obtained photocatalysts were named Pt/Cu(X)/T.

To check the effects induced by the employed metal deposition procedures and by the single metal or by the co-presence of Cu and Pt on the TiO_2 surface, three more samples were prepared, which were labelled T, DP/Cu(0.1)/T and Pt/T. Sample T was prepared by treating P25 TiO_2 according to the two above described steps, although in the absence of metal precursors. DP/Cu(0.1)/T was produced by Cu(II) grafting followed by the DP treatment (step B above) in the absence of Pt precursor. Pt/T was prepared by performing step A without the Cu(II) source, followed by Pt NPs deposition according to the DP method.

The effective amounts of Cu and Pt in the prepared samples were determined by inductively coupled plasma (ICP) atomic emission spectrometry, employing a Thermo Electron ICAP 6300 apparatus after microwave digestion of the photocatalysts in a 3:1 HCl/HNO_3 mixture. The expected nominal content of both metals was always confirmed by ICP analysis. For instance, in the case of Pt/Cu(0.1)/T, the Pt and Cu amounts were found to be (0.47 ± 0.04) and (0.09 ± 0.01) wt.%, respectively.

All chemicals employed in the preparation of the materials and of all solutions were purchased from Aldrich. Water purified by a Milli-Q water system (Millipore) was used throughout.

2.2. Photocatalysts characterization

X-ray powder diffraction (XRPD) patterns were recorded on a Philips PW3020 powder diffractometer, by using the Cu Kα radiation ($\lambda = 1.54056$ Å). Quantitative phase analysis was made by the Rietveld refinement method [26], using the "Quanto" software. The average anatase and rutile crystalline size was calculated by applying the Scherrer equation, from the width of the reflections at $2\theta = 25.4°$ and $2\theta = 27.4°$, respectively, calculated as the ratio between the peak area and the peak intensity obtained by fitting the XRPD profile with a Gaussian function.

The BET specific surface area (SSA) was measured by N_2 adsorption at liquid nitrogen temperature on a ASAP 2020 apparatus, after out-gassing *in vacuo* at 150 °C for at least 2 h. Diffuse reflectance (R) spectra of the photocatalyst powders were recorded on a Jasco

V-670 spectrophotometer equipped with a PIN-757 integrating sphere, using barium sulphate as a reference, and then converted into absorption (A) spectra (A = 1–R).

High resolution transmission electron microscopy (HRTEM) and high angular annular dark field images in scanning mode (STEM-HAADF) were taken on a JEOL FS2200-FEG instrument operating at 200 kV. The catalyst was dispersed in ethanol, dropped on a carbon-film coated gold grid and dried in air. In STEM and energy dispersive X-ray (EDX) analysis the spot size was 0.7 nm. The 3.7.0. analysis station with the JED-2200 software from Jeol was used to process EDX spectra.

X-band Continuous Wave EPR spectra were recorded on a Brucker EMX spectrometer equipped with a cylindrical cavity and operating at a 100 kHz field modulation. The measurements were carried out at the liquid nitrogen temperature in quartz cells that can be connected to a conventional high-vacuum apparatus (residual pressure < 10^{-4} mbar). The effects of UV and visible light on the EPR spectra were investigated by irradiating the sample in the EPR resonant cavity by means of a 1600 W mercury arc lamp (Oriel Instruments) equipped with a IR water filter to avoid over-heating and eventually with an additional 420 nm cut off filter, to exclude UV radiation.

X-ray absorption spectra (XANES and EXAFS) at both the Cu K-edge (8979 eV) and Pt L3-edge (11564 eV) were measured in the fluorescence mode using a Silicon Drift Detector (KETEK, model AXAS-A) at the SuperXas beamline of the Swiss Light Source (SLS) synchrotron. The proper amount of powder was mixed with cellulose and pressed in pellets. Three spectra were recorded for each sample at each edge, and merged in order to increase the signal to noise ratio. Reference Cu and Pt foils placed between the second and third ionization chamber were also measured for energy calibration. Bulk PtO_2, CuO, Cu_2O, $Cu(OH)_2$ and a $CuTi_2$ alloy were employed as reference materials. All spectra were analyzed and processed using the IFFEFIT software package [27], including Athena for spectral normalization, background subtraction, *k*-weighting, Fourier Transformation and linear combination analysis and Artemis for spectra fitting. Simulated Cu–Cu and Cu-Ti single scattering path EXAFS spectra at the Cu K-edge were calculated using the FEFF6 code [28]. Continuous Cauchy Wavelet Transform (CCWT) of the EXAFS spectra was performed using a Matlab script released by Muñoz et al. [29].

2.3. Photoactivity tests

The activity of the photocatalyst powders in hydrogen production by methanol photosteam reforming $CH_3OH + H_2O \rightarrow CO_2 + 3H_2$ was tested in a closed recirculation laboratory scale apparatus [8]. The photocatalyst powder (14 mg) was mixed with distilled water (1.2 mL), deposited on 0.85–0.42 mm quartz beads (3 g), and dried at 70 °C for 2 h. The so obtained photocatalyst bed was inserted into the photoreactor consisting of a flat cylindrical Plexiglas cell, frontally closed with a Pyrex glass optical window (irradiated surface *ca.* 20 cm^2), which was connected to a closed stainless steel system. After preliminary thorough purging with nitrogen to remove any trace of oxygen, the photocatalyst bed was continuously fed, at 40 mL min^{-1}, with a stream of N_2 saturated by the vapour of a 20 vol.% methanol−water solution (methanol molar fraction $x = 0.10$ in the liquid phase), kept at 30 °C. The absolute pressure of the reactor, 1.2 bar at the beginning of the runs, progressively increased during irradiation because of the accumulation of gas-phase products. During the runs, typically lasting 6 h in the case of the bare T sample, the recirculating gas was automatically sampled online every 30 min and injected into an Agilent 6890 N gas chromatograph (GC) equipped with two columns, two detectors (thermoconductivity and flame ionization), and a Ni-catalyst kit for CO and CO_2 methanation. N_2 was used as carrier gas. The GC

response was preliminarily calibrated for H_2, CO, and CO_2 analysis. When testing Pt/Cu(X)/T materials, purging with N_2 in the dark was required every 2 h, to avoid excessive accumulation of products in the recirculating gas phase. All kinetic tests were repeated at least two times. The irradiation source, always switched on 30 min prior the beginning of the run and placed 20 cm from the reactor, was a xenon arc lamp (LSH302, LOT Oriel, 300 W), having 40.0 mW cm^{-2} irradiation intensity, and operative in the 350–400 nm range, as measured with an optical power meter (Thorlabs PM200) equipped with a thermal power sensor (Thorlabs S302C).

3. Results and discussion

3.1. Photocatalysts characterization

3.1.1. XRPD and BET analyses

Identical XRPD patterns were obtained with all investigated materials [30], which demonstrates that both Cu(II) ions grafting and Pt NPs deposition did not affect the original crystalline phase composition of P25 TiO_2 (84% anatase – 16% rutile), in agreement with previous reports on noble metal modified titania [8,25,31,32]. Modified samples evidenced a 22.4 nm mean anatase crystallite size, which is slightly larger than that of unmodified P25 (21.0 nm), possibly due to the loss of fine particles during the surface modification procedures. Similarly, the mean rutile crystallite size underwent a slight increase, *i.e.* being 32.1 nm and 35.1 nm in the case of original P25 TiO_2 and modified T sample, respectively. No variation of the TiO_2 lattice parameters of any Pt/Cu(X)/T sample was observed, thus confirming that both Cu and Pt were just deposited on the TiO_2 surface, and not incorporated into the TiO_2 matrix [22,33,34].

BET analyses did not evidence any significant change in SSA of both reference samples and Pt/Cu(X)/T materials with respect to unmodified P25 TiO_2, all measured SSA ranging between 48 and 50 m^2 g^{-1}.
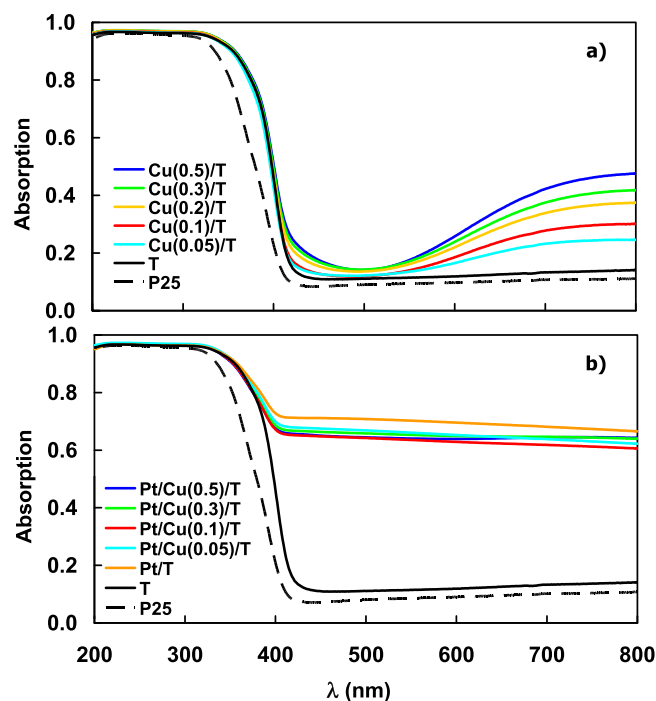

Fig. 1. UV–vis absorption spectra of the investigated Cu(X)/T samples (a) as-prepared and (b) after their surface modification with a fixed amount (0.5 wt.%) of Pt NPs. Absorption profiles obtained with commercial P25, T and Pt/T samples are also reported for comparison.

3.1.2. UV–vis diffuse reflectance spectra

Diffuse reflectance analyses indicate that Cu(II) grafting markedly enhanced the optical absorption of the materials in the visible light region. In fact, as shown in Fig. 1a, Cu(X)/T samples show an extra absorption in the 700–800 nm region, related to the Cu(II) *d-d* transition, and an absorption tail in the 400–500 nm region, which can be ascribed to the interfacial charge transfer (IFCT) of electrons from the valence band (VB) of TiO_2 to the grafted Cu(II) species [14].

The effects on the UV–vis absorption spectra induced by the subsequent Pt NPs deposition on the materials can be appreciated in Fig. 1b, where the absorption spectra of the T and Pt/T samples are also shown for comparison. Pt/Cu(X)/T materials, appearing as grey powders, exhibit a broad absorption in the whole visible region (400–800 nm). However, Cu and Pt containing samples absorb in the visible region slightly less than Pt/T. By considering that ICP measurements demonstrate that Pt/T and the Pt/Cu(X)/T samples contain the same amount of Pt (*i.e.* 0.47 ± 0.04 wt.%), this slight absorption decrease may possibly be related to the higher reflectance of copper.

Reference sample T (containing no metals) shows a slightly red-shifted absorption onset with respect to unmodified P25, compatible with the partial enlargement of the mean TiO_2 crystallite size induced by the impregnation route itself, also evidenced by XRPD analysis. This confirms that the route here employed to deposit relatively low amounts of Cu(II) species on the TiO_2 surface does not produce any intrinsic narrowing of the semiconductor band gap, which was observed, instead, when larger amounts of

CuO nanoclusters were deposited on TiO_2 by the chemisorption-calcination cycle technique [35].

3.1.3. STEM analysis

STEM-HAADF images of the Pt/Cu(0.5)/T sample, containing the largest nominal amount of grafted Cu(II), are shown in Fig. 2. TiO_2 appears in the form of NPs forming very close microaggregates, ranging from 10 to 50 nm in size, consistent with XRPD analysis. Moreover, a homogeneous distribution of platinum NPs can be appreciated, with size between 1 and 3 nm, appearing as bright spots deposited on TiO_2, due to the different Z-contrast of the noble metal with respect to the TiO_2 support. Cu species in the form of nanoaggregates cannot be distinguished, possibly because of the lower Z-contrast in comparison with that of platinum with respect to the predominant titanium in the TiO_2 matrix [22]. However, EDX analysis confirmed the presence of Cu both far and close to Pt NPs (Fig. 2d), which is compatible with the formation of small Cu clusters homogeneously anchored on the TiO_2 surface.

3.2. XAS analysis

The normalized X-ray absorption near edge structure (XANES) spectra at the Pt L3-edge of selected Pt/Cu(X)/T samples shown in Fig. 3A display an intense whiteline above the Pt L3-edge at an energy of 11.564 keV, which is intermediate between those of the reference Pt foil and bulk α-PtO_2. Thus, in all Pt/Cu(X)/T samples platinum is present in both metallic and oxidized state. The linear combination analysis of the spectra obtained with different
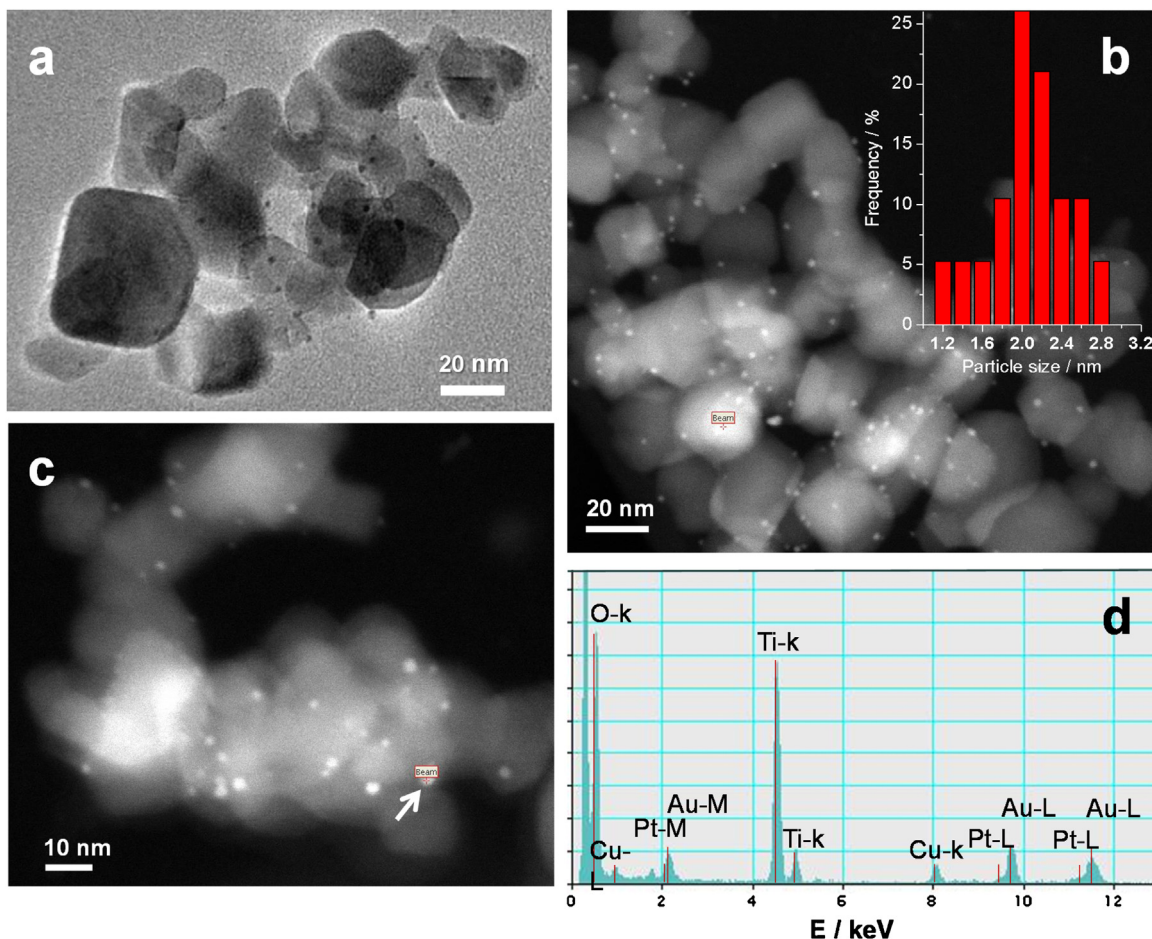

Fig. 2. (a) TEM and (b,c) STEM images of Pt/Cu(0.5)/T. The inset in (b) shows the noble metal particle size distribution. (d) EDX analysis performed on the point indicated by an arrow in (c).
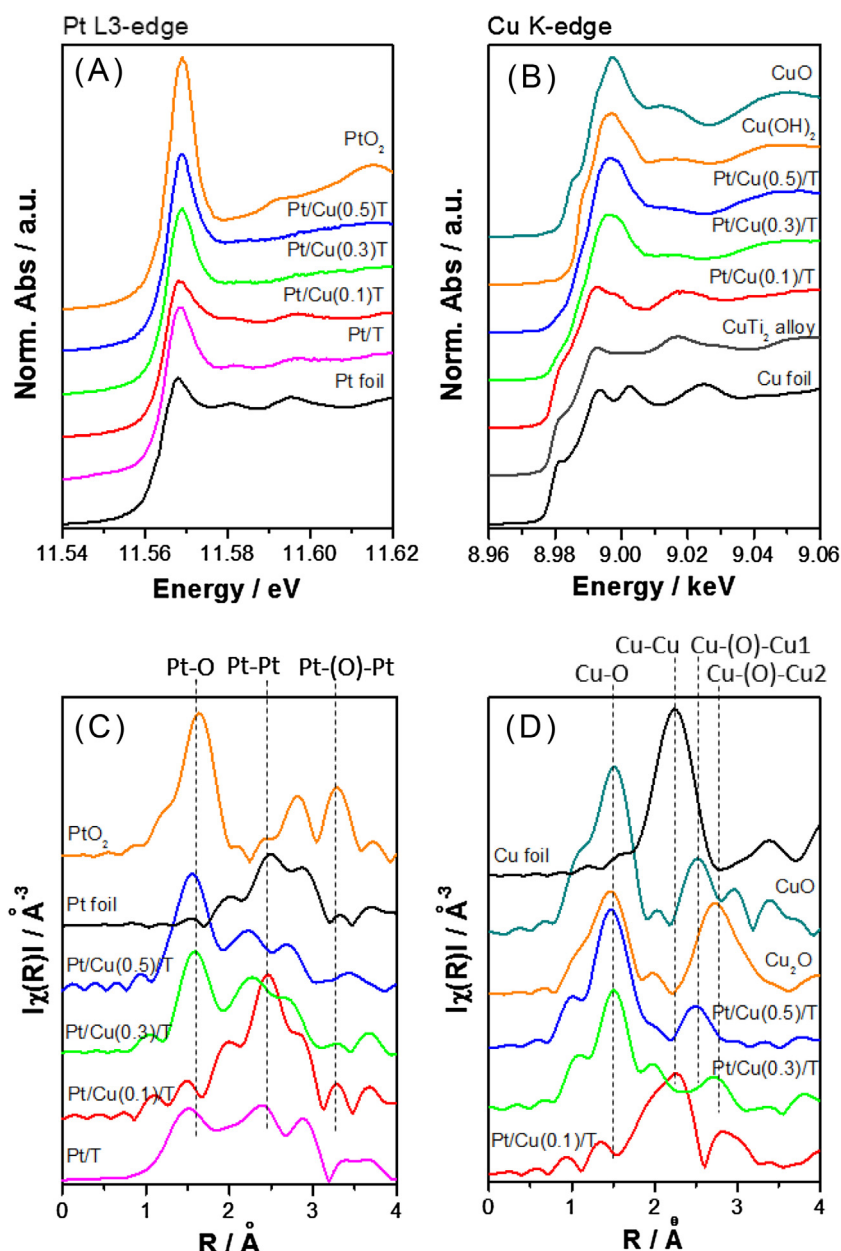
Fig. 3. (A, B) XANES and (C, D) k^2 FT-EXAFS spectra at the (A, C) Pt L3- and (B, D) Cu K- edges of the investigated samples. The FT-EXAFS spectra are not phase shift corrected.

samples, performed on the basis of the XANES spectra obtained with reference samples, shows that Cu(II) pre-grafting of the TiO_2 surface affects the percent amount of reduced Pt, as reported in Table 1. In particular, while *ca.* 73 wt.% of Pt is present in metallic state in Pt/T, Pt/Cu(0.1)/T contains the highest percent amount of metallic Pt (*ca.* 89 wt.%), which is much lower in the other two Pt- and Cu-containing samples, with the percent amount of oxidized Pt increasing with the amount of pre-grafted Cu(II) species.

The FT-EXAFS spectra at the Pt L3-edge of the investigated samples (Fig. 3C) show the presence of two signals centered at an interatomic distance R of *ca.* 1.6 Å and 2.5 Å, corresponding to the first Pt-O and Pt–Pt in metallic Pt coordination shells, respectively. In all spectra the second Pt-(O)-Pt coordination shell of PtO_2 at *ca.* $R = 3.2$ Å can hardly be distinguished. Moreover, the fitting of these FT-EXAFS spectra (Table 2) shows that *i*) the coordination number of the Pt-O shells are much lower than that of bulk PtO_2 (*ca.* 2 *vs.* 6, respectively), and *ii*) both the coordination number and the inter-atomic distance of the Pt–Pt shells of the metallic particles decrease with increasing amount of pre-grafted Cu(II). These results sug- gest that the Pt NPs consist of an oxidized surface layer covering a

Table 1
Results of the linear combination fitting of XANES spectra at the Cu K- and Pt L3-edges.

Sample	Cu(II)/wt.%	Cu(I)/wt.%	Cu(0)/wt.%	Pt(IV)/wt.%	Pt(0)/wt.%
Pt/T	–	–	–	27	73
Pt/Cu(0.1)/T	27	–	73	11	89
Pt/Cu(0.3)/T	79	19	2	37	63
Pt/Cu(0.5)/T	97	3	–	46	54

Table 2
Fitting results of the EXAFS spectra at the Pt L3-edge. CN = coordination number; R = inter-atomic distance; σ^2 = Debye Waller factor (mean square disorder); ΔE_0 = energy shift of the absorption edge; % R-factor = relative error of the fit and data. The amplitude reduction factor (S_0^2) was set at 0.74 for the Pt–Pt shell and at 0.79 for the Pt-O shell, as determined by fitting of the reference materials.

Sample	Shell	CN	R/Å	σ^2 (Å^2)	ΔE_0/eV	% R-factor
Pt foil	Pt-Pt	12[a]	2.766	0.0039	8.7	0.2%
Ref. PtO$_2$	Pt-O	6[a]	2.009	0.0024	10.5	0.4%
Pt/T	Pt-O	1.6	1.956	0.0044	6.2	1.7%
	Pt-Pt	9.2	2.743	0.0091		
Pt/Cu(0.1)/T	Pt-O	1.1	1.977	0.0174	7.7	2.1%
	Pt-Pt	9.2	2.738	0.0056		
Pt/Cu(0.3)/T	Pt-O	1.6	1.975	0.0004	8.6	5.4%
	Pt-Pt	7.3	2.719	0.0032		
Pt/Cu(0.5)/T	Pt-O	2.3	1.958	0.0029	6.9	3.2%
	Pt-Pt	6.5	2.710	0.0096		

[a] Set parameters.

metallic core and that the size of Pt NPs is influenced by the copper content, decreasing with increasing Cu(II) pre-grafted on TiO$_2$. This would explain the increase of Pt(IV) fraction with increasing copper content, as a higher fraction of oxidized surface Pt atoms is expected when Pt NPs are smaller and thus more highly dispersed on the TiO$_2$ surface.

The XANES spectra of the same samples at the Cu K-edge (Fig. 3B) together with their linear combination analysis (Table 1) show that in Pt/Cu(0.1)/T copper is predominantly in zero-valent form (73% Cu(0) and 27% Cu(II)), in Pt/Cu(0.3)/T it consists of a mixture of Cu(I) (19%) and Cu(II) (79%), while in Pt/Cu(0.5)/T the Cu(II) form largely prevails (97%). However, the shape of the XANES spectra shown in Fig. 3B significantly differs from those of both Cu foil and bulk CuO. In particular, the XANES spectra of both Pt/Cu(0.3)/T and Pt/Cu(0.5)/T are more similar to that of Cu(OH)$_2$. By considering that the shape of the XANES spectrum is affected, besides by the oxidation state, also by the chemical environment surrounding the absorber atom, this fact suggests that in such samples the coordination structure of Cu(II) is different with respect to that of CuO. Irie, et al. [14] also found that the XANES spectra of their 0.27%Cu-grafted/TiO$_2$ sample resembled that of Cu(OH)$_2$ and attributed this to a distorted CuO structure, where Cu(II) ions are coordinated with 5 oxygen atoms in a square pyramidal form, as in the case of Cu(OH)$_2$, rather than in the four-coordinated square planar form of crystalline CuO.

By contrast, the XANES spectrum of Pt/Cu(0.1)/T differs from that of the Cu foil and it mainly resembles that of the Cu-Ti alloy (Fig. 3B). In order to prove the presence of Ti in the coordination environment of Cu, the Continuous Cauchy Wavelet Transform (CCWT) was applied, which is able to distinguish neighboring atoms of different chemical nature but located at very similar interatomic distance R. In fact, even if originating similar FT-EXAFS spectra, the difference in the original $\chi(k)$ spectrum is highlighted by the presence in the CCWT contour graph of a trace that can be located in a

different k range along the x-axis but centered at the same R along the ordinate axis.

As shown in Fig. 4, the CCWT of the XAS spectra of both the simulated Cu–Cu scattering path (R = 2.5576 Å and σ^2 = 0.003 Å^2) and the Cu foil generate a trace in the contour graph with a maximum located in the 6 Å^{-1} < k < 8 Å^{-1} wavenumber range. By contrast, the maxima of the simulated Cu-Ti scattering path (R = 2.6399 Å and σ^2 = 0.003 Å^2) of the Cu-Ti alloy and of Pt/Cu(0.1)/T are all located at lower k values (5 Å^{-1} < k < 7 Å^{-1}). Hence, the CCWT analysis demonstrates the presence of Ti atoms in the coordination environment of Cu in Pt/Cu(0.1)/T. However, the formation of a Cu-Ti alloy should be excluded, by considering the here employed mild preparation conditions. On the other hand, the smaller average coordination number (CN) of the Cu–Cu shell obtained for Pt/Cu(0.1)/T with respect to the Cu foil (6 *vs.* 12) suggests that Cu is present as small aggregates of few atoms on the TiO$_2$ surface, with Cu atoms at the bottom of such clusters tightly coordinated to surface Ti atoms (Table 3).

XAS results thus suggest that during the grafting step Cu(II) species very likely adsorb on specific TiO$_2$ surface sites, creating clusters which are progressively larger with increasing Cu(II) amount. These Cu(II) agglomerates, homogeneously distributed on the TiO$_2$ surface, may be reduced to metal Cu during the treatment with NaBH$_4$ and then re-oxidized after exposure to air. However, in the low Cu-containing Pt/Cu(0.1)/T sample the small Cu clusters coordinate with surface Ti atoms forming a peculiar surface structure which stabilizes the metallic form of grafted copper.

3.3. EPR analysis

3.3.1. Investigation under dark conditions

EPR spectra of both Cu(X)/T and Pt/Cu(X)/T samples (with X = 0.1 and 0.5), recorded under vacuum and at liquid nitrogen temperature, are shown in Fig. 5. In the spectrum of bare P25 TiO$_2$, also

Table 3
Fitting results of the EXAFS spectra at the Cu K-edge. CN = coordination number; R = interatomic distance; σ^2 = Debye Waller factor (mean square disorder); ΔE_0 = energy shift of the absorption edge; % R-factor = relative error of the fit and data. The amplitude reduction factor (S_0^2) was set at 0.78 for the Cu–Cu shell and at 0.72 for the Cu-O shell as determined by fitting of the reference materials.

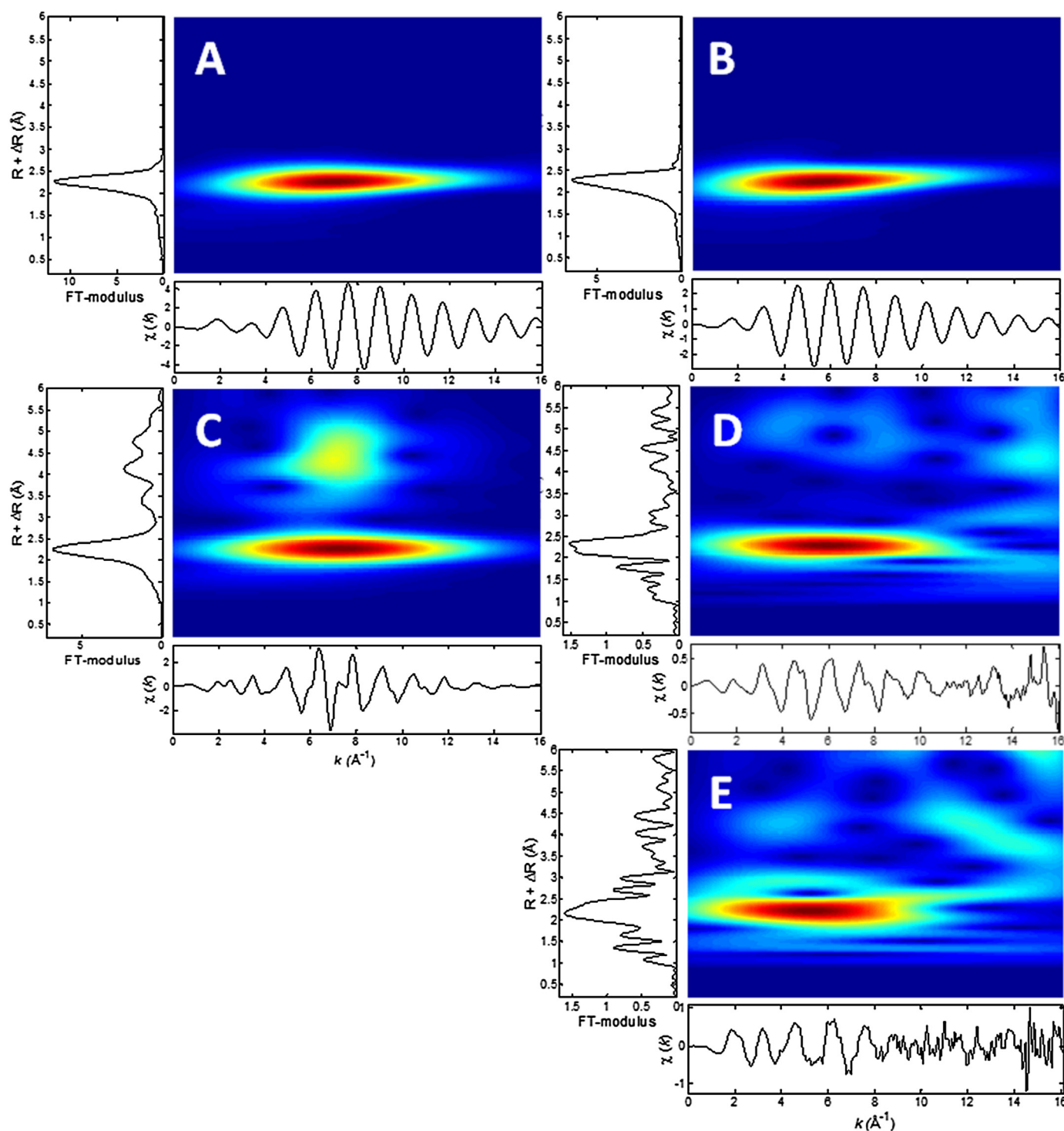| Sample	Shell	CN	R/Å	σ^2 (Å^2)	ΔE_0/eV	% R-factor
Cu foil	Cu-Cu	12[a]	2.542	0.0083	3.9	0.2%
Ref. Cu$_2$O	Cu-O	2[a]	1.841	0.0026	6.1	0.4%
	Cu-(O)-Cu2	12[a]	2.967	0.0272		
Ref. CuO	Cu-O	4[a]	1.965	0.0026	4.3	0.6%
Pt/Cu(0.1)/T	Cu-Cu	6.0	2.523	0.013	−0.7	6.1%
	Cu-Ti	1.2	2.712	0.001		
Pt/Cu(0.3)/T	Cu-O	2.6	1.952	0.003	1.7	5.8%
	Cu-(O)-Cu2	3.0	2.981	0.011		
Pt/Cu(0.5)/T	Cu-O	3.1	1.933	0.004	0.33	1.6%
	Cu-(O)-Cu2	3.8	2.760	0.015		

[a] Set parameters.

Fig. 4. Continuous Cauchy Wavelet Transform (CCWT) of the k^2 weighted $\chi(k)$ EXAFS spectra at the Cu K-edge of simulated (A) Cu–Cu and (B) Cu-Ti scattering paths, (C) Cu and (D) CuTi alloy foils, and (E) Pt/Cu(0.1)/T.

included for comparison in Fig. 5 (line a), a tiny signal amenable to trace of Ti^{3+} centres can be observed [36,37], which is typically originated from the intrinsic defects of the P25 material and is well documented in the literature [38,39].

All Cu(II) grafted samples (spectra b-e in Fig. 5) show a complex EPR signal, which is the fingerprint of Cu^{2+} species, the presence of which in different relative amount confirms the results of EXAFS analysis. Cu^{2+} is a 3d^9 ion (S = 1/2) with a non zero nuclear spin (^{63}Cu natural abundance 69.09% and ^{65}Cu natural abundance 30.91%,

I = 3/2). Its EPR features (**g** and hyperfine **A** tensors) are correlated to the d orbitals splitting and to the ground state of the cation, which in turn strictly depends on its geometrical and chemical environment. A 3d^9 ion such as Cu^{2+} undergoes Jan-Teller effect and is therefore usually found in axially distorted coordination. The expected g tensor for an isolated Cu^{2+} ion in axially distorted octahedral symmetry is based on a parallel component ($g_{//}$) higher than the free electron value ($g_{//} = g_z > g_e$) and characterized by a well-defined quartet of hyperfine lines (multiplicity 2 I + 1 = 4) having a typical $A_{//}$ splitting.
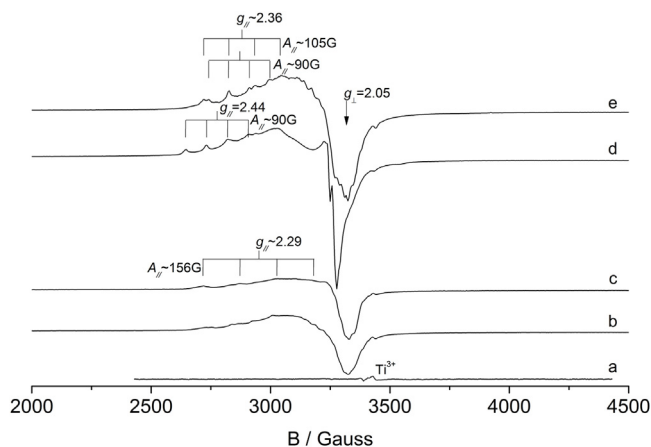
Fig. 5. CW-EPR spectra recorded at low temperature under vacuum condition. (a) Bare P25, (b) Cu(0.1)/T, (c) Pt/Cu(0.1)/T, (d) Cu(0.5)/T, (e) Pt/Cu(0.5)/T.

Fig. 6. CW-EPR spectra of Cu(0.1)/T recorded at low temperature under vacuum condition (black) and in the presence of 2 mbar of physisorbed O_2 (gray).

In the case of surface supported ions, the perpendicular g component ($g_\perp$, being $g_{//} > g_\perp > g_e$) often shows an unresolved hyperfine splitting due to the small value of this component ($A_\perp \ll A_{//}$). For example, in the case of surface Cu(II) species on TiO_2, g tensors with $g_{//} = 2.44$-2.32 and $g_\perp = 2.007$-2.005 and $A_{//}$ hyperfine coupling in the range 100–160 G are reported [40–42]. Instead, for isolated Cu(II) ions, possibly incorporated into a TiO_2 matrix, similar g factors were found but with hyperfine coupling constant of about 80–90 G [43,44]. The presence of totally unresolved signals is usually associated to strongly interacting (not isolated) Cu^{2+} centres [44].

In our case, all EPR spectra reported in Fig. 5 (lines b–e) are due to Cu^{2+} ions and can be interpreted as the overlap between a family of interacting sites, originating a broad and asymmetric EPR signal, and one or more families of isolated cupric ions, producing a hyperfine structure resolved in the parallel component ($A_{//}$). The materials containing 0.1 wt.% of Cu originate an EPR signal with $g_{//} \sim 2.29$, $A_{//} = 156$ G and an unresolved perpendicular region, thus showing a relative low content of isolated Cu(II) ions, the typical hyperfine structure of which is barely visible (Fig. 5b,c). Differently, in the case of higher Cu loading (i.e., 0.5 wt.%), isolated cupric ions are more abundant and distinct families of such ions can be distinguished on the basis of the parallel component characterized by $g_{//} = 2.44$ and $A_{//} \sim 90$ G (Fig. 5d) or by $g_{//} \sim 2.36$ with hyperfine coupling $A_{//}$ ranging from ~ 90 G to ~ 105 G (Fig. 5e). Pt/Cu(0.5)/T exhibits the better resolved EPR hyperfine structure.

The presence of a broad and featureless component is commonly observed in materials containing surface Cu^{2+} ions and can be explained by invoking both dipolar broadening and the presence of strong g strain. The first effect is due to the presence of clustered and interacting paramagnetic centres, while the second is related to the presence of a marked heterogeneity of coordination sites. Whatever the origin of such spectral feature, the obtained EPR signals (Fig. 5b,c) clearly indicate that in both Cu(0.1)/T and Pt/Cu(0.1)/T a fraction of grafted Cu(II) ions covers disordered regions, as amorphous areas of the material.

The EPR spectrum of a Cu(0.1)/T was recorded under oxygen atmosphere at liquid nitrogen temperature. In such conditions the dipolar interaction between the paramagnetic oxygen molecules in the physisorbed layer and the paramagnetic species present at the surface of the solid (Cu^{2+}, in this case) cause the spectrum of the latter species to vanish while the other centres (subsurface or bulk) are unaffected by this interaction. The EPR spectrum of Cu(0.1)/T acquired in the presence of physisorbed oxygen (Fig. 6, grey line) shows i) a decrease of the overall signal intensity, ii) a net decrease of the hyperfine structure corresponding to the isolated species
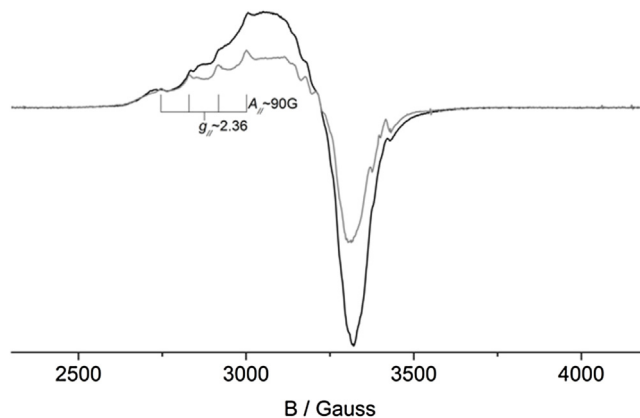
dominating the spectrum under vacuum ($g_{//} = 2.29$, $A_{//} = 156$) which must be, therefore, a surface exposed species and iii) the appearance of a new structure with four hyperfine lines ($g_{//} \sim 2.36$ and $A_{//} \sim 90$ G) which was buried in the spectrum recorded under vacuum (Fig. 6, black line) and that shows up only when the surface species is depressed by interaction with oxygen. This new species also observed for Cu(0.5)/T under vacuum conditions (Fig. 5d), corresponds to an isolated Cu(II) species, present also in the case of Cu(0.1)/T, and located under the surface.

EPR measurements thus demonstrate the presence of 2–3 families of isolated Cu^{2+} ions in all investigated samples, which are either exposed at the TiO_2 surface or entrapped on less exposed surface layers, together with more aggregated and ill-defined Cu^{2+} species in mutual dipolar interaction, which are the large majority of cupric ions grafted on TiO_2. The ratio between the two families of Cu(II) centres cannot be evaluated, due to the complexity of the EPR spectra. However, the EPR signal change observed in the presence of O_2 suggests that the aggregated Cu(II) centres originating a broad EPR signal are mainly distributed on the TiO_2 surface, while the majority of isolated Cu(II) ions are less prone to interact with physisorbed O_2 (and thus show a lower surface character).

3.3.2. Investigation under irradiation

The effects on the EPR response of Cu(0.1)/T and Pt/Cu(0.1)/T induced by irradiation with visible or UV–vis light were also studied. The intensity, obtained via double integration of the EPR spectra, of the signals acquired under vis or UV–vis irradiation, normalized with respect to that obtained in the dark, are reported in Fig. 7. All spectra were recorded at liquid nitrogen temperature under vacuum conditions.

For both materials irradiation produces an overall decrease of the EPR signal associated to Cu^{2+} species, which is more pronounced when light also included the UV component. The partial disappearance of the surface Cu^{2+} signal upon visible light irradiation ($\lambda > 420$ nm) is consistent with the expected activation of IFCT in such kind of Cu(II) grafted TiO_2 materials, i.e. electrons in the VB of TiO_2 are directly transferred to the discrete energy levels of Cu(II) ions and form EPR silent Cu(I), with positive holes remaining in the VB of TiO_2. Moreover, the fact that with Pt/Cu(0.1)/T the Cu^{2+} signal decrease attained upon visible light irradiation is lower than that observed in the case of Cu(0.1)/T is compatible with an interaction occurring between Cu and Pt, allowing back electron transfer from the photogenerated Cu(I) species to Pt NPs, with the subsequent restoring of Cu(II) species.

The larger Cu^{2+} intensity drop observed for both photocatalysts upon UV–vis irradiation with respect to visible light irradiation may be reasonably ascribed to the fact that under such conditions elec-
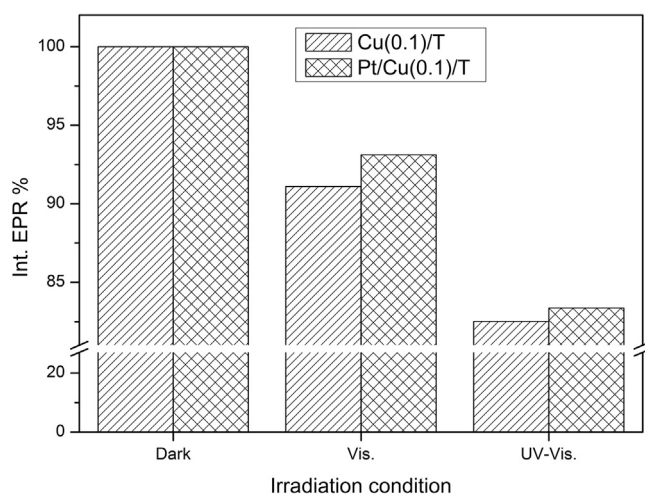
Fig. 7. EPR spectral intensity (associated to Cu^{2+} species) acquired after irradiation of Cu(0.1)/T and Pt/Cu(0.1)/T with visible ($\lambda > 420$ nm) or UV–vis light, compared to that obtained in the absence of light (dark conditions). All spectra were recorded at liquid nitrogen temperature with the samples kept under vacuum.

tron transfer from the VB of TiO_2 to Cu(II) may also proceed through TiO_2 band gap excitation followed by electron transfer from the TiO_2 CB to grafted Cu(II), in addition to the above mentioned IFCT mechanism. Moreover, grafted Cu(II) ions are expected to better

survive in the presence of surface Pt NPs, which may directly scavenge the electrons photopromoted into the TiO_2 CB, a process in competition with electron transfer to Cu^{2+} species, as supported by the EPR experiments reported in Fig. 7.

When similar experiments were performed in the presence of adsorbed oxygen the Cu^{2+} EPR intensity underwent only very minor decrease under irradiation. This demonstrates that photopromoted electrons preferentially react with O_2, a powerful electron scavenger, and are consequently less likely transferred to Pt nanoparticles or to Cu(II) grafted species. Also Nosaka et al. [41] observed no significant decrease of the Cu^{2+} EPR signal in the presence of O_2 under visible light and suggested that the eventually formed Cu^+ species may efficiently reduce O_2 molecules to form $O_2^{-\bullet}$ or H_2O_2 *via* a catalytic multielectron process, thus returning to original Cu^{2+}.

3.4. Photocatalytic activity

In the photocatalytic steam reforming reaction, hydrogen production is paralleled by methanol oxidation up to CO_2 through the formation of formaldehyde and formic acid as intermediate species; carbon monoxide and other minor side products are also produced [8]. In all photocatalytic tests H_2, CO_2 and CO evolution occurred at constant rate under full lamp irradiation, as in previous studies [8,45,46], whereas no hydrogen production was observed under visible light irradiation ($\lambda_{irr} > 420$ nm). Some examples of photocatalytic hydrogen production *vs.* irradiation time are

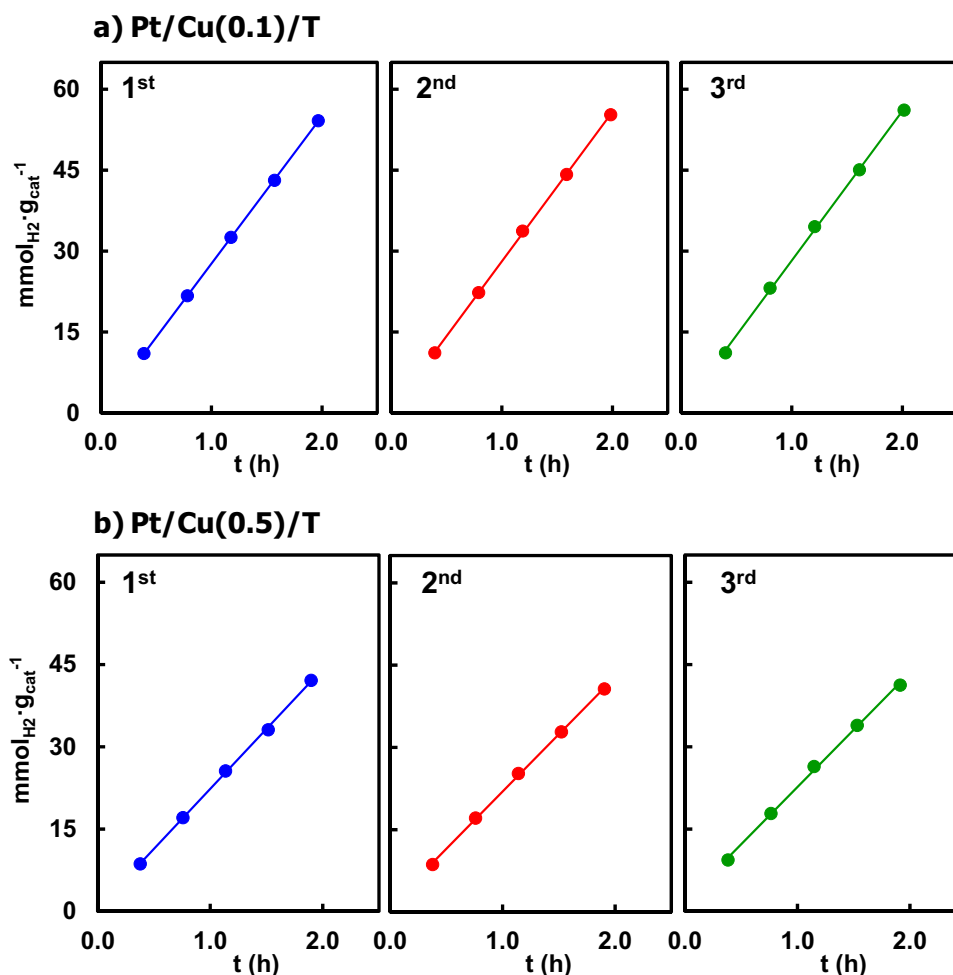**Fig. 8.** Subsequent time courses of photocatalytic hydrogen production obtained on (a) Pt/Cu(0.1)/T and (b) Pt/Cu(0.5)/T. Between each kinetic run, the photocatalytic bed was purged with N_2 in the dark in order to remove the large amount of products accumulated in the recirculating gas phase.
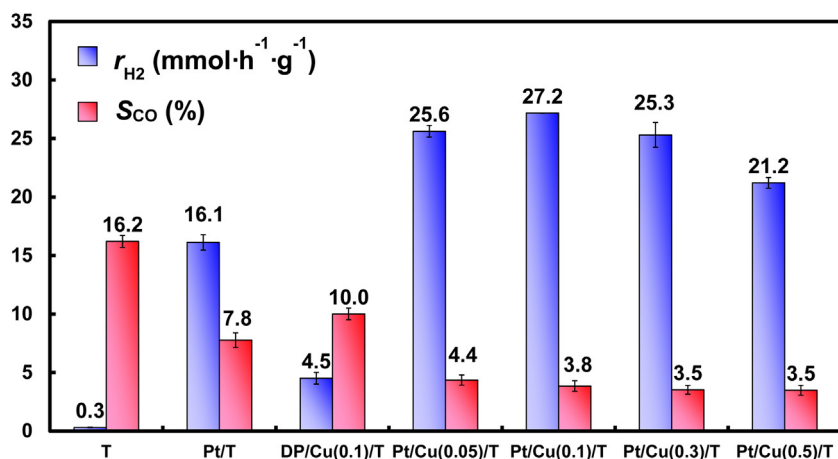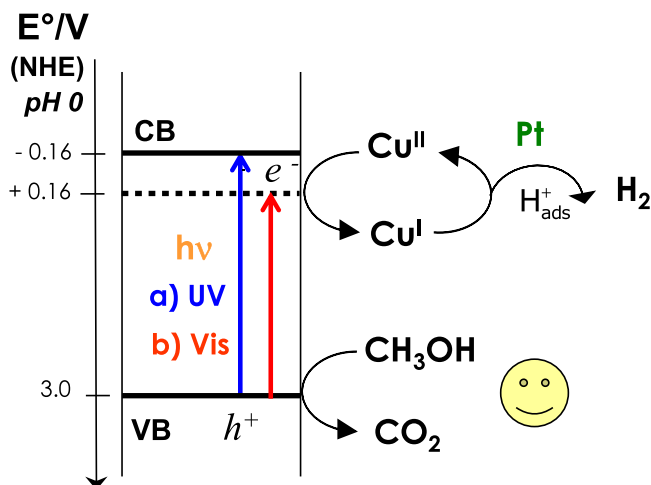
Fig. 9. Rates of H_2 production, r_{H2} (blue bars) and percent selectivity to CO, S_{CO} (red bars) attained with the Cu(II) pre-grafted Pt/TiO_2 samples during methanol photocatalytic steam reforming. Results obtained with reference T, Pt/T and DP/Cu(0.1)/T samples are also shown for comparison. (For interpretation of the references to colour in this figure legend, the reader is referred to the web version of this article.)

shown in Fig. 8. The rate of H_2 production, r_{H2}, and the percent selectivity to CO, S_{CO}, obtained with the here investigated photocatalysts are reported in Fig. 9, together with those obtained with reference naked TiO_2 (sample T) or reference samples obtained from P25 TiO_2 either by Cu grafting followed by reduction with $NaBH_4$ (DP/Cu(0.1)/T), or by Pt deposition (Pt/T). The r_{H2} values obtained with the Cu(X)/T photocatalysts series are all around $0.8 \, mmol \, h^{-1} \, g_{cat}^{-1}$ (not shown in Fig. 9), i.e. only slightly higher than that measured with reference T.

The rates of hydrogen production obtained with all photocatalysts of the Pt/Cu(X)/T series are the highest values ever measured within our laboratory scale recirculation photocatalytic system. They are higher than those obtained with photocatalysts prepared by Pt NPs deposition on TiO_2, or synthesized by flame spray pyrolysis [8], and also with flame-made fluorinated Pt/TiO_2 [47]. Moreover, a volcano-shaped photoactivity trend was obtained with increasing Cu content in the Pt/Cu(X)/T photocatalyst series (Fig. 9), the maximum rate of hydrogen production ($27.2 \, mmol \, h^{-1} \, g_{cat}^{-1}$) being attained with Pt/Cu(0.1)/T, containing 0.1 wt.% of copper. The r_{H2} value attained with this photocatalyst is higher than the sum of those obtained with DP/Cu(0.1)/T ($4.5 \, mmol \, h^{-1} \, g_{cat}^{-1}$) or Pt/T ($16.1 \, mmol \, h^{-1} \, g_{cat}^{-1}$). This highlights a very intriguing synergistic effect induced on photocatalytic hydrogen production by the co-presence of grafted Cu and Pt NPs on the TiO_2 surface.

Furthermore, Cu(II) pre-grafting on TiO_2 followed by Pt NPs deposition also affected the distribution of methanol oxidation products. In fact, as shown in Fig. 9, with all Pt/Cu(X)/T samples a significant drop in selectivity to CO was obtained, S_{CO} passing from 7.8% and 10% for Pt/T and DP/Cu(0.1)/T to 3.8% for best performing Pt/Cu(0.1)/T, while the selectivity to CO_2 with all Pt/Cu(X)/T photocatalysts remained almost constant, in the 37–41% range. The lower S_{CO} obtained with our Cu pre-grafted Pt/TiO_2 photocatalysts makes them very interesting in the perspective of directly feeding fuel cells with the hydrogen produced by photocatalytic steam reforming, because problems related to the undesired poisoning of Pt-Pd based catalysts of fuel cells would be mitigated.

The origin of the very high hydrogen production rate and of the synergistic effect on TiO_2 photoactivity induced by pre-grafting low amounts of Cu(II) species on the titania surface, followed by Pt NPs deposition and chemical reduction, may be explained in relation to the oxidation state and local surroundings of the two metals on the TiO_2 surface. We notice, in fact, that the treatment of the Cu grafted TiO_2 with $NaBH_4$, required to reduce platinum in Pt NPs, has beneficial effects on photoactivity. Indeed, the rate of hydrogen production obtained with reference DP/Cu(0.1)/T is much higher than

Scheme 1. Electron transfer paths, induced by UV or visible light irradiation, in the Cu(II) pre-grafted Pt/TiO_2 materials, based on the conduction band (CB) and valence band (VB) edges of TiO_2, in relation to the redox potential of the Cu^{2+}/Cu^+ couple.

that ($0.8 \, mmol \, h^{-1} \, g_{cat}^{-1}$) obtained with the photocatalysts of the Cu(X)/T series. On the other hand, the higher activity of Pt/Cu(X)/T photocatalysts with respect to bare (T) or Cu-modified DP/Cu(X)/T (see Fig. 9) can be easily related to the positive role of the noble metal, acting as trap of CB electrons, with a Schottky barrier formation and a consequently more efficient electron-hole separation [8].

During our photocatalytic steam reforming tests performed under *anaerobic conditions* the simultaneous charge transfer processes depicted in Scheme 1 may occur. Cu(II) ions in the pre-grafted Cu species can accept the electrons photopromoted to the TiO_2 CB under UV irradiation (path (a), blue arrow in Scheme 1), with an increase in electron-hole separation. At the same time, as suggested by Irie et al. [14,41,48], Cu(II) ions may directly accept electrons from the VB of TiO_2 by interfacial charge transfer (IFCT), which may occur also under visible light irradiation (see path (b), red arrow in Scheme 1). Indeed, our EPR analysis demonstrates that the amount of Cu^{2+} species decreases under irradiation, and that such decrease under UV irradiation is larger than under visible light, when only IFCT is possible (see Fig. 7). This confirms that both TiO_2 band gap excitation and IFCT activation are at work with copper-containing photocatalysts. Both of them produce holes in

the VB of TiO_2, favoring the full oxidation of methanol up to CO_2, with a consequent decrease of selectivity to CO.

The best photocatalytic performance was attained with Pt/Cu(0.1)/T, on which, as evidenced by EXAFS analysis, small CuO aggregates, intimately coordinated with Ti surface atoms, may coexist with metallic Cu, probably localized at the CuO – TiO_2 interface (see Table 1), which may favour all electron transfer paths. Indeed, low amounts of Ni(0), acting as ohmic contact at the interface between NiO nanoclusters and TiO_2, were recently found to play a role in increasing H_2 photocatalytic production from aqueous methanol solutions employing TiO_2 photocatalysts containing both Ni and Au [13]. On the other hand, photoinduced electron transfer to grafted Cu(II) may also lead to the *in situ* formation of metallic Cu, which can act as an efficient co-catalyst [15,16]. However, no induction period in H_2 production was observed at the beginning of our photocatalytic tests, which was instead observed by others [49] and attributed to Cu(II) photoinduced reduction to Cu(0). In fact, as shown in Fig. 8, three consecutive 2 h-long kinetic runs carried out with Pt/Cu(0.1)/T and Pt/Cu(0.5)/T demonstrate reproducible H_2 production, linearly increasing with time.

The slight photoactivity decrease observed in the Pt/Cu(X)/T series with increasing Cu loading (Fig. 9) may originate from the progressive enlargement of copper oxide deposits on the TiO_2 surface (as pointed out by EXAFS analysis in Section 3.2), more abundant and larger CuO clusters being expected to have weaker interaction with the TiO_2 surface [22,50]. At the same time the increase of Cu^{2+} component with increasing grafted copper content (see Table 1) may decrease its ability to generate hydrogen, in line with recent literature results [22].

Of course, the oxidation state of copper grafted onto TiO_2 may easily change, either during the photocatalyst treatment with $NaBH_4$ required to reduce Pt NPs, or by O_2 upon exposure to air leading to the formation of Cu_2O or CuO (Cu_xO) nanoclusters, besides during irradiation under anaerobic conditions (see EPR results in Fig. 7). If Cu_xO nanoclusters become crystalline *e.g.* by post-deposition thermal treatment, they behave as semiconductors with band gap energy ranging from 1.4 to 2.6 eV, depending on their size [51]. The so formed *p-n* heterojunction between TiO_2 and Cu_xO may contribute in increasing photoproduced charge carriers separation. In fact, under UV–vis light irradiation photopromoted electrons can be transferred from the CB of TiO_2 to the CB of CuO [18], which are located at −0.16 and +0.16 V *vs.* NHE (pH 0), respectively, while photogenerated holes might be trapped within the TiO_2 particles [34,52–54].

On the other hand, the simultaneous activation of TiO_2 and CuO under UV–vis irradiation may produce an accumulation of electrons in the CB of CuO, with a consequent shift of the Fermi level of CuO towards a more negative potential [55], *i.e.* more negative than the H^+/H_2 redox couple. By this way enough overvoltage would be attained to drive efficient H_2 evolution, likely occurring on Pt NPs, from CuO modified TiO_2 photocatalysts (see Scheme 1), thus accounting for beneficial Cu-Pt synergistic effects.

4. Conclusions

This work highlights the beneficial effects induced by Cu(II) pre-grafting on the activity of Pt/TiO_2 photocatalysts in H_2 production from methanol/water vapour mixtures up to unprecedentedly high H_2 production rates measured with our laboratory scale photocatalytic system. The highest photoactivity was obtained with a TiO_2-based photocatalyst containing 0.1 wt.% of copper, in which CuO nanoclusters appear to be intimately coordinated with surface Ti atoms in a surface structure that partially stabilizes pre-grafted copper in metallic form, possibly acting as an electron-transfer bridge at the interface between CuO nanoclusters and TiO_2, facilitating electron-hole separation. Synergistic effects on photoactivity in hydrogen production are thus induced by the co-presence of Cu nanoclusters obtained through mild grafting and Pt NPs on the TiO_2 surface. The so obtained Cu nanoclusters guarantee a proper switching of the copper oxidation state under UV–vis irradiation, which facilitates electron transfer to adsorbed protons.

References

[1] Y. Ma, X.L. Wang, Y.S. Jia, X.B. Chen, H.X. Han, C. Li, Chem. Rev. 114 (2014) 9987–10043.
[2] S.S. Yi, J.M. Yan, B.R. Wulan, S.J. Li, K.H. Liu, Q. Jiang, Appl. Catal. B Environ. 200 (2017) 477–483.
[3] M. Wu, J.-M. Yan, X.-W. Zhang, M. Zhao, Q. Jiang, J. Mater. Chem. A 358 (2015) 15710–15714.
[4] M. Bowker, Catal. Lett. 142 (2012) 923–929.
[5] T. Kawai, T. Sakata, Nature 286 (1980) 474–476.
[6] A. Yamakata, T. Ishibashi, H. Onishi, J. Phys. Chem. B 107 (2003) 9820–9823.
[7] P.V. Kamat, J. Phys. Chem. B 106 (2002) 7729–7744.
[8] G.L. Chiarello, M.H. Aguirre, E. Selli, J. Catal. 273 (2010) 182–190.
[9] Z. Hai, N. El Kolli, D.B. Uribe, P. Beaunier, M. José-Yacaman, J. Vigneron, A. Etcheberry, S. Sorgues, C. Colbeau-Justin, J. Chen, H. Remita, J. Mater. Chem. A 1 (2013) 10829.
[10] M.G. Méndez-Medrano, E. Kowalska, A. Lehoux, A. Herissan, B. Ohtani, D. Bahena, V. Briois, C. Colbeau-Justin, J.L. Rodríguez-López, H. Remita, J. Phys. Chem. C 120 (2016) 5143–5154.
[11] Y. Qu, X. Duan, Chem. Soc. Rev. 42 (2013) 2568–2580.
[12] S. Oros-Ruiz, R. Zanella, S.E. Collins, A. Hernández-Gordillo, R. Gómez, Catal. Commun. 47 (2014) 1–6.
[13] A.L. Luna, E. Novoseltceva, E. Louarn, P. Beaunier, E. Kowalska, B. Ohtani, M.A. Valenzuela, H. Remita, C. Colbeau-Justin, Appl. Catal. B Environ. 191 (2016) 18–28.
[14] H. Irie, K. Kamiya, T. Shibanuma, S. Miura, D.A. Tryk, T. Yokoyama, K. Hashimoto, J. Phys. Chem. C 113 (2009) 10761–10766.
[15] T. Sreethawong, S. Yoshikawa, Catal. Commun. 6 (2005) 661–668.
[16] H.J. Choi, M. Kang, Int. J. Hydrogen Energy 32 (2007) 3841–3848.
[17] J. Bandara, C.P.K. Udawatta, C.S.K. Rajapakse, Photochem. Photobiol. Sci. 4 (2005) 857–861.
[18] J. Yu, Y. Hai, M. Jaroniec, J. Colloid Interface Sci. 357 (2011) 223–228.
[19] M.K. Jeon, J. Park, M. Kang, J. Ind. Eng. Chem. 13 (2007) 84–91.
[20] V. Gombac, L. Sordelli, T. Montini, J.J. Delgado, A. Adamski, G. Adami, M. Cargnello, S. Bernal, P. Fornasiero, J. Phys. Chem. A 114 (2010) 3916–3925.
[21] S.J.A. Moniz, J. Tang, ChemCatChem 7 (2015) 1659–1667.
[22] M. Jung, J. Scott, Y.H. Ng, Y. Jiang, R. Amal, Int. J. Hydrogen Energy 39 (2014) 12499–12506.
[23] M. Jung, J.N. Hart, D. Boensch, J. Scott, Y.H. Ng, R. Amal, Appl. Catal. A Gen. 518 (2016) 221–230.
[24] Y. Shiraishi, H. Sakamoto, Y. Sugano, S. Ichikawa, T. Hirai, ACS Nano 7 (2013) 9287–9297.
[25] M.V. Dozzi, L. Prati, P. Canton, E. Selli, Phys. Chem. Chem. Phys. 11 (2009) 7171–7180.
[26] H.M. Rietveld, J. Appl. Cryst. 2 (1969) 65–71.
[27] B. Ravel, M. Newville, J. Synchrotron Radiat. 12 (2005) 537–541.
[28] S.I. Zabinsky, J.J. Rehr, A. Ankudinov, R.C. Albers, M.J. Eller, Phys. Rev. B 52 (1995) 2995–3009.
[29] M. Muñoz, P. Argoul, F. Farges, Am. Miner. 88 (2003) 694–700.
[30] I. Grigioni, M.V. Dozzi, M. Bernareggi, G.L. Chiarello, E. Selli, Catal. Today 281 (2017) 214–220.
[31] X.Z. Li, C. He, N. Graham, Y. Xiong, J. Appl, Electrochem 35 (2005) 741–750.
[32] M. Mrowetz, A. Villa, L. Prati, E. Selli, Gold Bull. 40 (2007) 154–160.
[33] K. Lalitha, G. Sadanandam, V.D. Kumari, M. Subrahmanyam, B. Sreedhar, N.Y. Hebalkar, J. Phys. Chem. C 114 (2010) 22181–22189.
[34] X. Qiu, M. Miyauchi, K. Sunada, M. Minoshima, M. Liu, Y. Lu, D. Li, Y. Shimodaira, Y. Hosogi, Y. Kuroda, K. Hashimoto, ACS Nano 6 (2012) 1609–1618.
[35] Q. Jin, M. Fujishima, A. Iwaszuk, M. Nolan, H. Tada, J. Phys. Chem. C 117 (2013) 23848–23857.
[36] S. Livraghi, M. Chiesa, M.C. Paganini, E. Giamello, J. Phys. Chem. C 118 (2011) 25413–25421.

[37] S. Livraghi, M. Rolando, S. Maurelli, M. Chiesa, M.C. Paganini, E. Giamello, J. Phys. Chem. C 118 (2014) 22141–22148.
[38] D.C. Hurum, A.G. Agrios, K.A. Gray, T. Rajh, M.C. Thurnauer, J. Phys. Chem. B 107 (2003) 4545–4549.
[39] I. Fenoglio, G. Greco, S. Livraghi, B. Fubini, Chem.– A Eur. J. 15 (2009) 4614–4621.
[40] G. Li, N.M. Dimitrijevic, L. Chen, T. Rajh, K.A. Gray, J. Phys. Chem. C 112 (2008) 19040–19044.
[41] Y. Nosaka, S. Takahashi, H. Sakamoto, A.Y. Nosaka, J. Phys. Chem. C 115 (2011) 21283–21290.
[42] A.A. Altynnikov, L.T. Tsikoza, V.F. Anufrienko, J. Struct. Chem. 47 (2006) 1161–1169.
[43] G. Còrdoba, M. Viniegra, J.L.G. Fierro, R. Arroyo, J. Solid State Chem. 138 (1998) 1–6.
[44] T.C. Ensign, T.-T. Chang, A.H. Kahn, Phys. Rev. B. 188 (1969) 703–709.
[45] G.L. Chiarello, A. Di Paola, L. Palmisano, E. Selli, Photochem. Photobiol. Sci. 10 (2011) 355–360.
[46] G.L. Chiarello, D. Ferri, E. Selli, J. Catal. 280 (2011) 168–177.
[47] G.L. Chiarello, M.V. Dozzi, M. Scavini, J.-D. Grunwaldt, E. Selli, Appl. Catal. B Environ. 160–161 (2014) 144–151.
[48] M. Liu, X. Qiu, M. Miyauchi, K. Hashimoto, Chem. Mater. 23 (2011) 5282–5286.
[49] Z. Xi, C. Li, L. Zhang, M. Xing, J. Zhang, Int. J. Hydrogen Energy 39 (2014) 6345–6353.
[50] J. Yu, J. Ran, Energy Environ. Sci. 4 (2011) 1364.
[51] Y. Ge, Z.H. Shah, C. Wang, J. Wang, W. Mao, S. Zhang, R. Lu, ACS Appl. Mater. Interfaces 7 (2015) 26437–26444.
[52] M. Liu, R. Inde, M. Nishikawa, X. Qiu, D. Atarashi, E. Sakai, Y. Nosaka, K. Hashimoto, M. Miyauchi, ACS Nano 8 (2014) 7229–7238.
[53] M. Liu, K. Sunada, K. Hashimoto, M. Miyauchi, J. Mater. Chem. A 3 (2015) 17312–17319.
[54] T. Morikawa, Y. Irokawa, T. Ohwaki, Appl. Catal. A Gen. 314 (2006) 123–127.
[55] F. Teng, M. Chen, N. Li, X. Hua, K. Wang, T. Xu, ChemCatChem 6 (2014) 842–847.